On Weak Lensing Response Functions

D. Munshi[a,b,1]**, R. Takahashi**[c,2]**, J. D. McEwen**[b,3]

[a] *Imperial Centre for Inference and Cosmology (ICIC) & Astrophysics group,*
Imperial College, Blackett Laboratory, Prince Consort Road, London SW7 2AZ, UK
[b] *Mullard Space Science Laboratory, University College London,*
Holmbury St Mary, Dorking, Surrey RH5 6NT, UK
[c] *Faculty of Science and Technology, Hirosaki University,*
3 Bunkyo-cho, Hirosaki, Aomori, 036-8561, Japan

E-mail: [1]D.Munshi@ucl.ac.uk, [b]takahasi@hirosaki-u.ac.jp
[3]Jason.McEwen@ucl.ac.uk

ABSTRACT: We introduce the response function approach to model the weak lensing statistics in the context of separate universe formalism. Numerical results for the RFs are presented for various semi-analytical models that includes perturbative modelling and variants of halo models. These results extend the recent studies of the Integrated Bispectrum and Trispectrum to arbitrary order. We find that due to the line-of-sight projection effects, the expressions for RFs are not identical to the squeezed correlation functions of the same order. We compute the RFs in three-dimensions using the spherical Fourier-Bessel formalism which provides a natural framework for incorporating photometric redshifts, and relate these expressions to tomographic and projected statistics. We generalise the concept of k-cut power spectrum to k-cut response functions. In addition to response functions, we also define their counterparts in real space, since they are easier to estimate from surveys with low sky-coverage and non-trivial survey boundaries.

KEYWORDS: Cosmology, Large-Scale Structure, Weak Lensing

Contents

1 Introduction

The current generation of weak lensing surveys [1, 2] including the Subaru Hypersuprimecam survey[1](HSC) [3], Dark Energy Survey[2](DES)[4], Dark Energy Spectroscopic Instruments (DESI)[3], Prime Focus Spectrograph[4], KiDS[5] are already able to put cosmological constraints that are competitive with recent Cosmic Microwave Background surveys. The near-future Stage-IV large scale structure (LSS) surveys such as *Euclid*[5][6], Rubin Observatory[6][7] and Roman Space Telescope[8] will improve the constraints by an order-of-magnitude and provide answers to many of the questions that cosmology is facing. These will provide answers to many outstanding cosmological questions, including but not limited to, nature of dark matter (DM), dark energy (DE), possible modifications of General Relativity (GR) on cosmological scales [9, 10] and the sum of the neutrino masses [11].

---

[1]http://www.naoj.org/Projects/HSC/index.html
[2]https://www.darkenergysurvey.org/
[3]http://desi.lbl.gov
[4]http://pfs.ipmu.jp
[5]http://sci.esa.int/euclid/
[6]http://www.lsst.org/lsst home.shtml

Weak lensing observations target the relatively low-redshift ($z \sim 1$) universe and small scales where the perturbations are in the nonlinear regime and their statistics are non-Gaussian [1, 2, 12]. Indeed, understanding higher-order statistics is important as they can significantly reduce the degeneracy in cosmological parameters[13]. Nevertheless, higher-order statistics beyond the bispectrum and trispectrum are known to be difficult to model analytically, and in perturbation theory higher-order contributions becomes increasingly intractable as the order increases. Analytical modelling of the weak lensing three-point correlation function was initiated in real-space in [13, 14], and parallel development in the harmonic domain was initiated in [15, 16]. For early detection of non-Gaussianity see [17].

Another strand of work has involved designing and optimising estimators of non-Gaussianity. The numerical estimators are computationally demanding to implement. In addition, higher-order estimators are typically noise-dominated on small scales and cosmic variance dominated on large scales. A large number of simulations are required to accurate characterization [18]. Many different estimators have recently been proposed which probe the higher-order statistics of weak lensing maps [19]. These include the well-known real-space one-point statistics such as the cumulants [20] or their two-point correlators also known as the cumulant correlators as well as the associated PDF [21] and the peak-count statistics [22]. In the harmonic domain the estimators such as the Skew-Spectrum[23], Integrated Bispectrum [24] kurt-spectra [25], morphological estimator [26], integrated trispectrum [27], Betti number [28], extreme value statistics [29], position-dependent PDF [30], density split statistics [31], response function formalism [32], statistics of phase [34–36], estimators for shapes of the lensing bispectrum [33] are some of the statistical estimators and formalism recently considered by various authors in the context of understanding cosmological statistics in general and weak lensing in particular. In recent years approaches based on machine learning have also been employed [37].

The higher-order correlation functions are difficult to estimate from numerical simulations or observational data. In recent years the squeezed limits of higher-order correlation functions have been studied by many authors. These squeezed limits are also known as the response functions. Theoretical predictions of squeezed higher-order spectra are computed using separate universe simulations. From the data analysis perspective, the response functions are computed using exactly the same method employed for estimation of, e.g., Integrated Bispectrum, i.e., by dividing the survey volume/area into smaller regions and cross-correlating the local power spectrum against the local average of a given statistics. This gives an estimate of the global squeezed correlation functions. However, before applying to all-sky simulations and/or observational data, analytical results can also be compared with Separate Universe (SU) simulations.

The primary aim of this paper is to introduce the SU framework in the context of weak lensing studies using the response function approach. We will use this statistic to probe non-Gaussianity in weak lensing maps in projection (2D) as well as in three dimensions (3D). We will show due to projection effects, the response functions are not identical to the higher-order correlation functions in the squeezed limit but are closely related.

All previous works have focussed on three-dimensions (3D) response functions of the
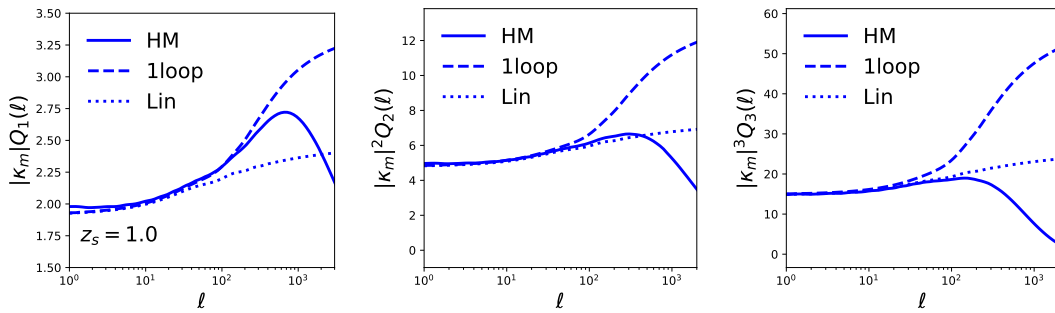
Figure 1: The response functions $|\kappa_m|^N Q_N$ defined in Eq.(3.11) are shown. From left to right panels depict $N = 1, 2$ and $N = 3$. The source redshift is $z_s = 1$. Various line styles correspond to different analytical models, linear, one-loop and halo model as indicated (see text for details).

density contrast δ. We will extend these results to weak lensing surveys in projection as well as to weak lensing in 3D. Our results relate the weak lensing convergence response functions Q_n to the underlying matter response function R_n. The response functions R_n probe the squeezed configurations of higher-order statistics and can be related to the derivative of the matter power spectrum $P(k)$ w.r.t. the local linear density contrast. In an analogus manner the response functions Q_n for weak lensing convergence κ are related to the squeezed higher-order spectra κ and can be linked to the high-order derivatives of angular power spectrum $\mathcal{C}_\ell$.

This paper is arranged as follows. In §1 we introduce our notations, next, in §2 we introduce the relevant concepts of weak lensing. The formalism of response functions in the context of separate Universe formalism in §3. In §4 we develop the response functions for the weak lensing. The response functions for k-cut correlation functions are presented in §5. The results are discussed in §6 and conclusions and future prospects are presented in §7.

The cosmological model parameters used are the Planck2015 best-fit flat ΛCDM model [39]: $h = 0.6727$, $\Omega_b = 0.0492$, $\Omega_m = 0.3156$, $\Omega_\Lambda = 0.6844$, $n_s = 0.9645$ and $\sigma_8 = 0.831$.

2   Weak Lensing Convergence in Projection

The projected (2D) weak lensing convergence κ is a line-of-sight integration of the underlying three-dimensional (3D) cosmological density contrast δ. The $\kappa(\boldsymbol{\theta})$ at a position $\boldsymbol{\theta}$ can be expressed as follows:

$$\kappa(\boldsymbol{\theta}, z_s) := \int_0^{r_s} dr W(r) \delta(r, \boldsymbol{\theta}); \tag{2.1a}$$

$$W(r) := \frac{3\Omega_M}{2} \frac{H_0^2}{c^2} a^{-1} \frac{d_A(r) d_A(r_s - r)}{d_A(r_s)}. \tag{2.1b}$$

We will suppress the variables r_s unless we consider the case where the sources are not confined in a single source plane. Here $d_A(r)$ is the comoving angular diameter distance at a comoving distance r, i.e., $\kappa(\boldsymbol{\theta}, z_s) \equiv \kappa(\boldsymbol{\theta})$ and $W(r.r_s) \equiv W(r)$. The kernel $W(r)$ encodes geometrical dependence; a is the scale factor, H_0 is the Hubble constant and Ω_M is the cosmological density parameter. $d_A(r)$ and $d_A(r_s)$ are comoving angular diameter distances at a comoving distances r and r_s. We have assumed all sources to be at a single source plane at a distance r_s. The projected lensing power spectrum $\mathcal{C}_\ell$ is given in the Limber and Born approximations by:

$$\mathcal{C}_\ell = \int_0^{r_s} dr \frac{W^2(r)}{d_A^2(r)} P_\delta\left(\frac{\ell}{d_A(r)}; r\right). \tag{2.2}$$

The tomographic power spectrum $\mathcal{C}_\ell^{ij}$ is given by restricting the line-of-sight integration for sources in a particular estimated redshift bins (labelled by i, j):

$$\mathcal{C}_\ell^{ij} = \int_0^{r_s} dr \frac{W_i(r)W_j(r)}{d_A^2(r)} P_\delta\left(\frac{\ell}{d_A(r)}; r\right). \tag{2.3}$$

the kernels W_i and W_j can be obtained by replacing r_s in Eq.(2.1b) respectively by r_{si} and r_{sj}. The upperlimit of integration will be $r_s = min(r_{si}, r_{sj})$.

Throughout, we assume that all sources are located at a single redshift. For a distribution of source redshifts there is a further radial integration.

$$\mathcal{C}_\ell = \int_0^{r_{max}} dr \frac{\hat{W}^2(r)}{d_A^2(r)} P_\delta\left(\frac{\ell}{d_A(r)}; r\right). \tag{2.4}$$

$$\kappa(\boldsymbol{\theta}) = \int_0^\infty n(z_s)\kappa(\boldsymbol{\theta}, z_s)dz_s \quad = \int_0^{r_{max}} dr \hat{W}(r)\delta(r); \tag{2.5}$$

$$\hat{W}(r) = \int_{z_s}^\infty dz_s W(r, r_s)n(z_s). \tag{2.6}$$

The integral along the radial direction takes into account contribution from individual source planes and $n(z_s)$ number density of sources at a source redshift z_s. We will ignore any noise due to intrinsic ellipticity distribution.

3 Separate Universe Formalism and Response Functions in Projection

In a SU formalism an infinite wavelength linear density perturbayion $\delta_L = D_+\delta_{L0}$ is considered. Here D_+ is the linear growth and δ_{L0} is the amplitude of the perturbation at a redshift $z = 0$. The amplitude δ_{L0} is constant over the SU simulation. For a real survey the entire survey is divided into large enough sub-volumes where δ_{L0} can still be considered constant (infinite wavelength). The resulting background matter density δ_ρ is absorbed by redefining the cosmological parameters (e.g., [40, 41]). We will denote the comoving coordinate, scale-factor, comoving wave number, and power spectrum respectively as $\mathbf{x}$, $a(t)$, k and $P(k)$. The

corresponding quantities in the modified cosmology will be denoted as $\tilde{\mathbf{x}}$, $\tilde{a}(t)$, $\tilde{k}$ and $\tilde{P}(\tilde{k})$. We will also introduce δ_a and δ_ρ the Lagrangian and Eulerian perturbation as follows:

$$\mathbf{x}a(t) = \tilde{\mathbf{x}}\tilde{a}(t); \quad 1 + \delta_a = \frac{\tilde{a}(t)}{a(t)} \tag{3.1a}$$

$$(1 + \delta_\rho) = (1 + \delta_a)^{-3}. \tag{3.1b}$$

$$\tilde{\Omega}_M \tilde{h}^2 = \Omega_M h^2 \tag{3.1c}$$

$$\tilde{x} = (1 + \delta_a)^{-1}x; \qquad \tilde{k} = (1 + \delta_a)k. \tag{3.1d}$$

Following the derivation in [38] We can expand δ_a and δ_ρ in terms of the linear overdensity $\delta_L = D_+\delta_{L0}$: The evolution of δ_a and δ_ρ in the fiducial cosmology can be solved using a spherical collapse model. The resulting equations are further simplified by assuming an Einstein de Sittter (EdS) background cosmology. The accuracy of such approximations have been tested and was found to be better than a few percents (see [38] for more details).

$$\delta_a = \sum_{n=1}^{\infty} e_n[\delta_L]^n; \quad \delta_\rho = \sum_{n=1}^{\infty} f_n[\delta_L]^n; \tag{3.2a}$$

$$e_i = \left\{ -1/4, -1/21, -23/1701, \cdots \right\} \tag{3.2b}$$

$$f_i = \left\{ 1, 17/21, 341/567, \cdots, \right\} \tag{3.2c}$$

The time dependence of δ_a and δ_ρ is implicit in their dependence on δ_L. The power spectrum in modified cosmology will be denoted as $\tilde{P}_\delta$ and in the fiducial cosmology by P_δ are related by the following expression:

$$P_\delta(k|\delta_L) = [1 + \delta_\rho]\tilde{P}_\delta([1 + \delta_a]k). \tag{3.3}$$

The growth-only response function is denoted by G_n and the total response function by R_n.

$$\tilde{P}_\delta(k, t) = \sum_{n=0}^{\infty} \frac{\delta_L^n}{n!} G_n(k, t) \, P_\delta(k, t); \tag{3.4a}$$

$$P_\delta(k, t|\delta_L) = \sum_{n=0}^{\infty} \frac{\delta_L^n}{n!} R_n(k, t) \, P_\delta(k, t). \tag{3.4b}$$

The nth-order response function for the density contrast is given by the nth-order derivative of the power spectrum with the linearly extrapolated overdensity δ_{L0}. A normalisation is also introduced by the power spectrum which renders the response function dimensionless.

$$R_n(k, t) = \frac{1}{P_\delta(k, t)} \frac{d^n P_\delta(k, t|\delta_L)}{d\delta_L^n(t)} \bigg|_{\delta_L=0}; \tag{3.5a}$$

$$G_n(k, t) = \frac{1}{P_\delta(k, t)} \frac{d^n \tilde{P}_\delta(k, t)}{d\delta_L^n(t)} \bigg|_{\delta_L=0}. \tag{3.5b}$$
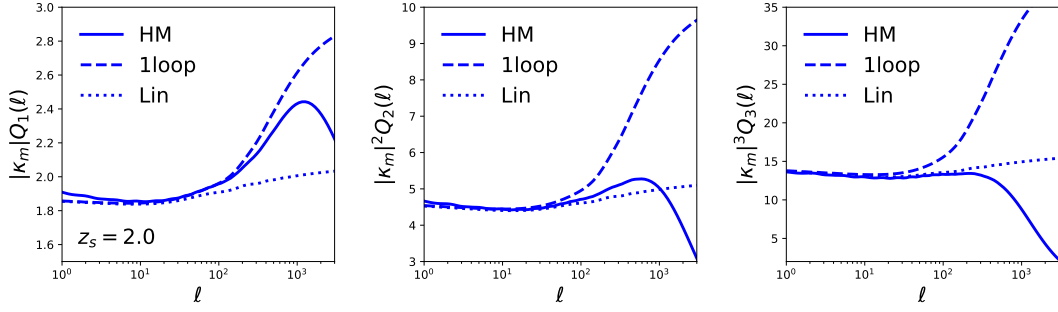
Figure 2: Same as Fig.1 but for source redshift $z_s = 2$.

The response functions can be recovered by Taylor expanding Eq(3.3). Next, we will focus on response function for the power spectrum of the weak lensing convergence. We will express these response functions in terms of the 3D response function for matter power spectrum.

The 2D power spectrum is given by:

$$\mathcal{C}_\ell(\kappa_L) = \int_0^{r_s} dr \frac{W^2(r)}{d_A^2(r)} P_\delta\left(\frac{\ell}{d_A(r)}; r \Big| \delta_L\right). \tag{3.6}$$

We will refer to this as the local angular power spectrum. The global angular power spectrum is recovered by taking $\delta_L = 0$ which leads to $\kappa_L = 0$ and we recover Eq.(2.4). Using Eq.(3.4a) we can write:

$$\mathcal{C}_\ell(\kappa_L) = \sum_{n=0}^{\infty} \frac{1}{n!} [\delta_{L0}]^n \int_0^{r_s} dr \frac{W^2(r)}{d_A^2(r)} R_n\left(\frac{\ell}{d_A(r)}, r\right) [D_+(r)]^n P_\delta\left(\frac{\ell}{d_A(r)}, r\right). \tag{3.7}$$

Using the following notation:

$$\kappa_L = \delta_{0L} |\kappa_m|; \quad \kappa_m = -\int_0^{r_s} dr D_+(r) W(r); \tag{3.8}$$

Notice this amounts to assuming δ_{0L} is same at all redshift and is a global parameter. Individual SU simulations will have a fixed δ_{0L}. Big enough patches of the real sky that evolve separately as SU can have different δ_L in our formalism. One of the objective of SU is to probe how the power spectra changes as a function of the local overdensity. where δ_L is the local over(under)-density and corresponding projected convergence is κ_L

$$\mathcal{C}_\ell(\kappa_L) = \sum_{n=0}^{\infty} \frac{1}{n!} \left[\frac{\kappa_L}{|\kappa_m|}\right]^n \int_0^{r_s} dr \frac{W^2(r)}{d_A^2(r)} R_n\left[\frac{\ell}{d_A(r)}, r\right] [D_+(r)]^n P_\delta\left(\frac{\ell}{d_A(r)}, r\right). \tag{3.9}$$

We introduce the response functions for the 2D, $\mathcal{Q}_n(\ell)$, through:

$$\mathcal{C}_\ell(\kappa_L) = \sum_{n=0}^{\infty} \frac{1}{n!} \mathcal{Q}_n(\ell) \kappa_L^n \mathcal{C}_\ell \tag{3.10}$$

Comparing Eq.(4.8) with Eq.(3.9) we deduce that:

$$Q_n(\ell) = \frac{1}{\mathcal{C}_\ell} \frac{1}{|\kappa_m|^n} \int_0^{r_s} dr \frac{W^2(r)}{d_A^2(r)} R_n \left[\frac{\ell}{d_A(r)}, r \right] [D_+(r)]^n P_\delta \left(\frac{\ell}{d_A(r)}, r \right).$$ (3.11)

The response function for cross-correlation of two different tomographic bins denoted by indices i and j can be derived similarly. We start from the definition of local cross-spectra:

$$\mathcal{C}_\ell^{ij}(\kappa_{LX}) = \int_0^{r_s} dr \frac{W^i(r)W^j(r)}{d_A^2(r)} P_\delta \left(\frac{\ell}{r}; r \middle| \delta_L \right) \qquad \kappa_{LX} \equiv [\kappa_{im}\kappa_{jm}]^{n/2}$$ (3.12)

We will later define the local cross-spectra in terms of κ_{LX} which is a geometric mean of κ_{mi} and κ_{mj} i.e. κ_m of the tomographic bins i and j respectively. Mathematically,

$$\kappa_{iL} = \delta_{L0}|\kappa_{im}|; \quad \kappa_{im} = -\int_0^{r_s} dr\, D_+(r)\, W_i(r);$$ (3.13)

The response functions $\mathcal{Q}_n^{ij}(\ell)$ for cross-spectra involving two tomographic is expressed as:

$$\mathcal{C}_\ell^{ij}(\kappa_{LX}) = \sum_{n=0}^{\infty} \frac{1}{n!} \, \mathcal{Q}_n^{ij}(\ell) \, \kappa_{LX}^n \mathcal{C}_\ell^{ij};$$ (3.14)

Combining Eq.(5.5) and Eq.(3.12)

$$Q_n^{ij}(\ell) = \frac{1}{\mathcal{C}_\ell^{ij}} \frac{1}{|\kappa_{LX}|^n} \int_0^{r_s} d\tilde{r} \frac{W^i(r)W^j(r)}{d_A^2(r)} R_n \left[\frac{\ell}{d_A(r)}, r \right] [D_+(r)]^n P_\delta \left(\frac{\ell}{d_A(r)}, r \right).$$ (3.15)

Throughout, we have used Limber approximation. The FFTlog based approach is often used to go beyond the Limber approximation [43] in the modelling of projected power spectrum. It is possible to incorporate a similar method to model the low-ℓ behaviour of the response functions. The expressions above are derived for single source plane. For generalisation to a source distribution specified by $n(z)$ we need to replace $W(z)$ in Eq.(3.6), Eq.(3.11) and other equations by $\hat{W}(z)$ as defined in Eq.(2.6). The definition of κ_m in Eq.(3.8) similarly will have to be modified.

Figure 1 and 2 respectively. The details of our results will be discussed in §6

Next, from [38] we have used the following expressions:

$$R_0(k) = 1; \tag{3.16a}$$

$$R_1(k) = f_1 + e_1 \frac{kP'(k)}{P(k)} + G_1(k); \tag{3.16b}$$

$$\frac{1}{2}R_2(k) = f_2 + e_2 \frac{kP'(k)}{P(k)} + e_1^2 \frac{k^2 P''(k)}{2P(k)} + \frac{1}{2}G_2(k) + f_1 G_1(k)$$
$$+ f_1 e_1 \frac{kP'(k)}{P(k)} + e_1 \frac{kP'(k)}{P(k)} G_1(k) + e_1 k G_1'(k); \tag{3.16c}$$

$$\frac{1}{6}R_3(k) = f_1 G_1(k) e_1 \frac{kP'(k)}{P(k)} + f_3 + \frac{G_3(k)}{6} + e_3 \frac{kP'(k)}{P(k)} + f_1 \frac{G_2(k)}{2} + f_1 e_2 \frac{kP'(k)}{P(k)}$$
$$+ f_1 e_1^2 \frac{k^2 P''(k)}{2P(k)} + f_2 G_1(k) + f_2 e_1 \frac{kP'(k)}{P(k)} + (f_1 e_1 + e_2)k G_1'(k) + e_1^2 \frac{k^2 G_1''(k)}{2}$$
$$+ e_1 k \frac{G_2'(k)}{2} + e_1^2 \frac{kP'(k)}{P(k)} k G_1'(k) + e_1^3 \frac{k^3 P'''(k)}{6P(k)} + 2e_1 e_2 \frac{k^2 P''(k)}{2P(k)}$$
$$+ e_1 \frac{kP'(k)}{P(k)} \frac{G_2(k)}{2} + G_1(k) \left(e_2 \frac{kP'(k)}{P(k)} + e_1^2 \frac{k^2 P''(k)}{2P(k)} \right). \tag{3.16d}$$

Notice that Eq.(3.16a)-Eq.(3.16d) are derived using a spherical collapse model of a given patch of the universe characterised by a linear over(under) density δ_L. For convergence studies which directly probe the underlying density contrast δ the response of halo occupancy distributions are not important, but in case of magnification studies they may have to take into account [42]. The expressions are the leading order terms in δ_L. Next-to-leading order corrections can also be computed by extending the series expansion beyond leading order. However this has no bearing on the modelling of the local power spectrum $P(k)$ which can be fully nonlinear. For the purpose of this paper we consider the halo model. We also present results for linear and from second-order correction as references. Many improvements of the halo model are discussed in the literature which can also be used in predicting the $P(k)$. In our notation $\hat{D}_+(t)$ represents the linear growth rate. The growth only response functions, denoted as G_n, takes a particularly simpler form when computed using linear theory.

Notice that the response functions $R_n(k)$ take a rather simpler form when we approximate the power spectrum locally as a power law. In this case, we can write $P(k) \propto k^n$ which leads us to $kP'(k)/P(k) = n$ and $k^2 P''(k)/P(k) = n(n-1)$, and to a good approximation the growth rate $G(k)$ is scale-independent.

$$G_n = \frac{1}{D_+^2} \frac{d^n \tilde{D}_+^2}{d\delta_L^n}\bigg|_{\delta_L=0}; \tag{3.17a}$$

$$\tilde{D}_+(t) = D_+(t) \sum_{n=0}^{\infty} g_n[\delta_L]^n; \tag{3.17b}$$

$$g_{n=0,1,2,3,4} = \{1, 13/21, 71/189, \cdots\}; \tag{3.17c}$$

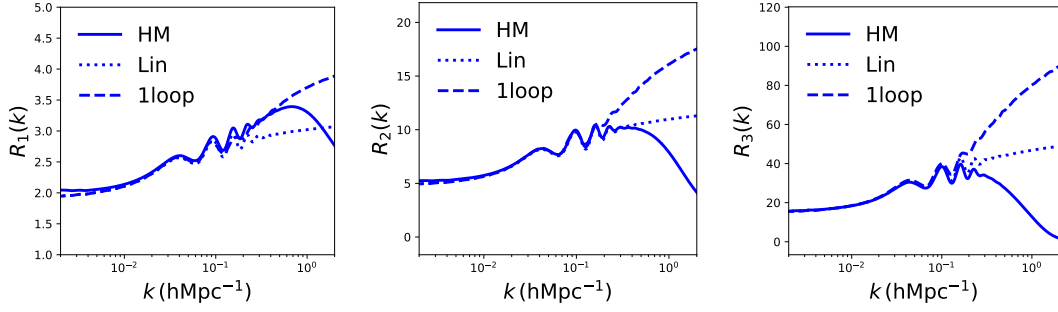$$G_{n=0,1,2,3,4} = \{1, 26/21, 3002/1323, \cdots\}. \tag{3.17d}$$

Figure 3: The response functions R_N defined in Eq.(3.16b)-Eq.(3.16d) are shown. From left to right panels depict $N = 1, 2$ and $N = 3$. The simulation redshift is at $z_s = 1$. Various line styles correspond to different analytical models, linear, one-loop and halo model as indicated (see text for details).

In the linear theory Eq.(3.3) takes the following form for the linear power spectrum local P_L and the fiducial power spectrum $P_{lin,fid}$:

$$P_L(k, t|\delta_L) = (1 + \delta_\rho(t)) \left(\frac{\tilde{D}_+(t)}{D_+(t)} \right)^2 \tilde{P}_{L,fid}([1 + \delta_a(t)]k, t). \tag{3.18}$$

Next, we turn our attention to a perturbative quasilinear calculation of response functions. The response functions for the density contrast δ are related to the angle averaged squeezed limits of correlation functions S_{N-2}^δ defined as follows:

$$S_{N-2}^\delta(k, k', k_1, \cdots k_{N-2}) = \int \frac{d\hat{\Omega}_1}{4\pi} \cdots \int \frac{d\hat{\Omega}_{N-2}}{4\pi} \langle \delta(\mathbf{k})\delta(\mathbf{k}')\delta(\mathbf{k}_1) \cdots \delta(\mathbf{k}_{N-2}) \rangle'. \tag{3.19a}$$

$$R_{N-2}(k) = \lim_{k_i \to 0} \frac{S_{N-2}(k, k', k_1, \cdots k_{N-2})}{P_L(k_1) \cdots P_L(k_{N-2})} \tag{3.19b}$$

Notice that $S_{N-2}^\delta(k, k', k_1, \cdots k_{N-2})$ is only non-zero when $k = k'$ in the limit $k_i \to 0$. Here, $d\hat{\Omega}_i = \sin\theta_i d\phi_i$. The angles $\hat{\Omega}_i = (\theta_i, \phi_i)$ are the angles associated with wave vector $\mathbf{k}$ and P_L is the linear power spectrum. We have used following shorthand notation above:

$$\langle \delta(\mathbf{k})\delta(\mathbf{k}')\delta(\mathbf{k}_1) \cdots \delta(\mathbf{k}_{N-2}) \rangle' = (2\pi)^3 \delta_{2D}(\mathbf{k}_1 + \cdots + \mathbf{k}_{N-2})$$
$$\times \langle \delta(\mathbf{k})\delta(\mathbf{k}')\delta(\mathbf{k}_1) \cdots \delta(\mathbf{k}_{N-2}) \rangle \tag{3.20}$$

Here, δ_{nD} represents the n-dimensional Dirac delta function. In case of 2D convergence or κ similarly we have:

$$S_{N-2}^\kappa(\ell, \ell', \ell_1, \cdots \ell_{N-2}) = \int \frac{d\theta_1}{2\pi} \cdots \int \frac{d\theta_1}{2\pi} \langle \kappa(\mathbf{l})\kappa(\mathbf{l}')\kappa(\mathbf{l}_1) \cdots \kappa(\mathbf{l}_{N-2}) \rangle'. \tag{3.21a}$$

$$Q_{N-2}(\ell) = \lim_{\ell_i \to 0} \frac{S_{N-2}^\kappa(\ell, \ell', \ell_1, \cdots \ell_{N-2})}{\mathcal{C}_{\ell_1}^\kappa \cdots \mathcal{C}_{\ell_{N-2}}^\kappa}. \tag{3.21b}$$
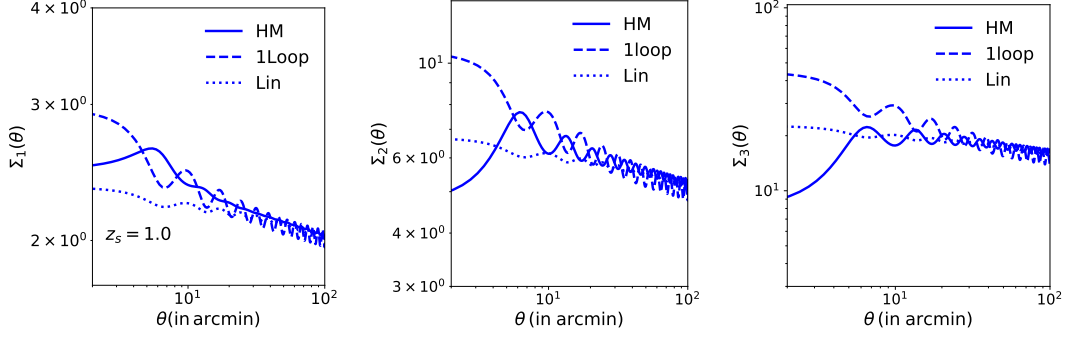
Figure 4: The response functions Σ_N defined in Eq.(3.29c) are shown for the source redshift $z_s = 1.0$. From left to right panels depict $N = 1, 2$ and $N = 3$. Various line styles correspond to different analytical models, linear, one-loop and halo model as indicated.

In the above expression θ_i is the polar angle of the vector $\mathbf{l}_i$ and $\ell_i = |\mathbf{l}_i|$. Notice also $S^\kappa_{N-2}(\ell, \ell', \ell_1, \cdots \ell_{N-2})$ is only non-zero when $\ell = \ell'$ in the limit $\ell_i \to 0$. The power spectrum $\mathcal{C}^\kappa_{\ell_1}$ is the linear convergence power spectrum for the same source distribution. The following notation was used:

$$\langle \kappa(\mathbf{l})\kappa(\mathbf{l}')\kappa(\mathbf{l}_1) \cdots \kappa(\mathbf{l}_{N-2})\rangle' = (2\pi)^2 \delta_{2\mathrm{D}}(\mathbf{l}_1 + \cdots + \mathbf{l}_{N-2})$$
$$\times \langle \kappa(\mathbf{l})\kappa(\mathbf{l}')\kappa(\mathbf{l}_1) \cdots \kappa(\mathbf{l}_{N-2})\rangle \tag{3.21c}$$

Here, Eq.(3.21a)-Eq,(3.21c) correspond to flat-sky approximations. The projected higher-order squeezed spectra are not identical to the projected response functions of same order. See for exact perturbative results in Appendix-§A

3.1 Beyond Linear Theory - Loop Corrections

In the standard perturbation theory (SPT) the power spectrum at a redshift z has the following expression (e.g., [12]):

$$P^{\mathrm{SPT}}(k) = D_+^2 P_L(k) + D_+^4 P^{1-\mathrm{loop}}(k) + D_+^6 P^{2-\mathrm{loop}}(k) + \cdots \tag{3.22}$$

Here $P^{1-\mathrm{loop}}$ $P^{2-\mathrm{loop}}$ denote loop-level corrections to the linear power spectrum P_L. In the previous section we used the linear power spectrum for computing the response functions. Perturbative corrections to the linear theory as given in Eq.(3.22) can improve these predictions when used in association with Eq.(3.16c)-Eq.(3.16d).

While Eq.(3.16a)-Eq.(3.16d) are derived using $\delta_L \ll 1$ this doesn't restrict the nature of the local power spectrum that can be used to compute the response functions. The perturbative nature of linear and 1-loop power spectrum is used here as a reference. Both linear and 1-loop power spectrum are expected to expected to diverge at low k. To improve convergence it is possible to include higher-order loop corrections or consider counter terms prescribed in Effective Field Theory (EFT).

3.2 Halo Model Response Functions

Next, we compute the response functions in a halo model. We will use the universal halo profile from Ref.[44]. We use the halo mass function by Tinker et al.[45]. For halo bias we use [46, 47], and finally we use the prescription by [48] for halo concentrations.

We introduce the following notation:

$$I_m^n(k_1, \cdots, k_m) \equiv \int d\ln M\, n(\ln M) \left(\frac{M}{\bar{\rho}}\right)^m b_n(M) u(M|k_1) \cdots u(M|k_m). \qquad (3.23)$$

Here $b_n(M)$ is the n-th order bias and $u(M|k_1)$ is the Fourier transform of the halo profile and k_i are the wave numbers. The power spectrum in the halo model has two contributions known as the 1-halo and 2-halo contribution $P_{1h}(k)$ and $P_{1h}(k)$ [50]:

$$P_{\mathrm{HM}}(k) = P_{2h}(k) + P_{1h}(k); \qquad (3.24a)$$

$$P_{2h}(k) = [I_1^1(k)]^2 P_{\mathrm{L}}(k); \quad P_{1h}(k) = I_2^0(k, k). \qquad (3.24b)$$

Following Ref.([49]) we can write the position-dependent 1-halo contribution as [50]:

$$P_{1h}(k, t|\delta_{L0}) = \sum_{n=0}^{\infty} \frac{1}{n!} I_2^n(k, k, t)[\hat{\delta}_L]^n. \qquad (3.25a)$$

The 2-halo contribution is similarly given by [50]:

$$P_{2h}(k, t, |\delta_{L0}) = \left(\sum_{n=0}^{\infty} \frac{1}{n!} f_n[\delta_L]^n\right) [\hat{\delta}_L]^n$$

$$\times \left(\sum_{n=0}^{\infty} \frac{1}{n!} I_1^{n+1}(k, t)[\delta_L]^n\right) P_{lin} \left[\left(\sum_{n=0}^{\infty} \frac{1}{n!} e_n[\delta_L]^n\right) k\right]. \qquad (3.26)$$

Finally, the response functions in the halo model are given by [38]:

$$R_1^{\mathrm{HM}}(k) = \left[f_1 + 2g_1 + e_1 \frac{d\ln P(k)}{d\ln k}\right] P_{2h}(k, t) + I_2^1(k, k, t); \qquad (3.27a)$$

$$R_2^{\mathrm{HM}}(k) = \left[2f_2 + 2f_1 g_1 + (f_1 + 2g_1)e_1 \frac{d\ln P(k)}{d\ln k}\right.$$

$$\left. +2g_1^2 + 4g_2 + 2e_2 \frac{d\ln P(k)}{d\ln k} + e_1^2 \frac{k^2}{P} \frac{d^2 P(k)}{dk^2}\right] P_{2h}(k, t) + I_2^2(k, k, t). \qquad (3.27b)$$

Notice these results correspond to the traditional halo model which uses the standard tree-level perturbation theory. Recently, a prescription to incorporate EFT based results in halo model [51] was proposed. Such corrections when included in halo model and 1-loop power spectrum in Eq.(3.22) can improve the agreement between the two models at high k.

The discrepancy seen at low k in R_N may be a result of not imposing mass conservation in a halo model as was pointed out in [52]. It is possible to replace $P_{\mathrm{L}}(k)$ in Eq.(3.24b) with $P^{\mathrm{SPT}}(k)$ defined in Eq.(3.22). This will make HM models to match SPT predictions up to
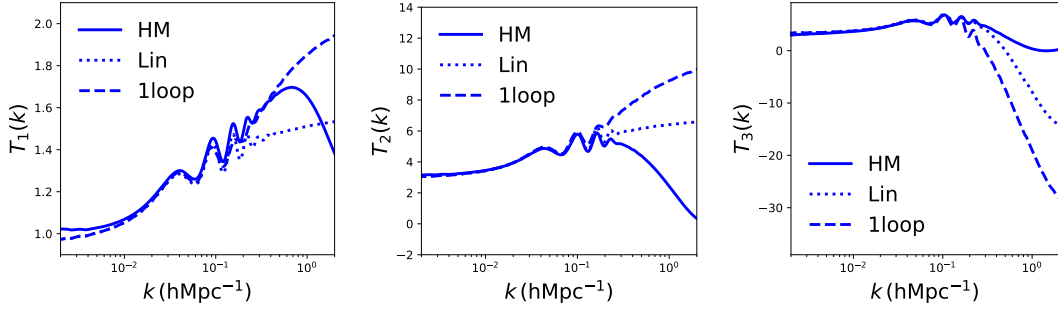
Figure 5: The parameters T_N for redshift $z = 0$ defined in Eq.(4.4a) - Eq.(4.4c) are plotted as a function the wave number k. From left to right panels depict $N = 1, 2, 3$. Various line styles correspond to different analytical models, linear, one-loop and halo model as indicated (see text for details).

scales comparable to the halo size where the 1-halo term takes over. This will improve the agreement between 1-loop results and halo model based predictions of response functions.

The values of the coefficients e_i, f_i and g_i are derived in [38]. The $n-$th order response function we have derived correspond to the Lagrangian density contrast δ_a and is generally denoted as R_n^L to distinguish it from the Eulerian response function related to density contrast δ_ρ. The conversion between the Lagrangian and Eulerian response functions is given by:

$$R_1^E(k) = R_1^L(k); \tag{3.28a}$$

$$R_2^E(k) = R_2^L(k) - 2f_2 R_1^L(k); \tag{3.28b}$$

$$R_3^E(k) = R_3^L(k) - 6f_2 R_2^L(k) + 6(2f_2^2 - f_3)R_1(k). \tag{3.28c}$$

We have computed the Lagrangian projected response functions Q_N by using the 3D Lagrangian response function $R_1^L(k)$. However, the projected Eulerian response functions can be computed using $R_1^E(k)$ in a straight forward manner. In addition to the perturbation theory and halo model based results, as mentioned above, the response functions can also be computed using the Effective Field Theory (EFT) predictions for the power spectrum [53].

Our numerical results for R_N for the redshift $z = 0$ are presented in Figure-3.

3.3 Response Functions for Two-point Correlation Function

In this section we will extend the results derived above to real space and derive the response functions for the two-point correlation function: $\xi(\theta_{12}) \equiv \langle \kappa(\boldsymbol{\theta})\kappa(\boldsymbol{\theta} + \boldsymbol{\theta_{12}}) \rangle$. Isotropy and homogeneity dictates $\xi(\theta_{12})$ only depends on the separation $\theta_{12} = |\boldsymbol{\theta_{12}}|$. For surveys with small sky-coverage and masks with non-trivial topology, response functions defined for two-point correlation function are easier to implement [54–56]. We begin by defining the local

estimate of the two-point correlation function (2PCF) $\xi(\theta_{12})$ as

$$\xi(\theta_{12}|\kappa_L) = \frac{1}{4\pi} \sum_{\ell=0}^{\ell_{max}} (2\ell+1)P_\ell(\cos\theta_{12})\mathcal{C}_\ell(\kappa_L) \approx \frac{1}{2\pi} \sum_{\ell=0}^{\ell_{max}} \ell J_0(\ell\theta_{12})\mathcal{C}_\ell(\kappa_L) \quad (3.29a)$$

Here P_ℓ is the Legendre polynomial of order ℓ. The second equality is valid only in the flat-sky approximation. Here, J_0 denotes the Bessel functions of the first kind of zeroth-order.

The corresponding global two-point correlation function $\xi(\theta)$ can be recovered by replacing the local power spectrum $\mathcal{C}_\ell(\kappa_L)$ with its global counterpart $\mathcal{C}_\ell$. The n-th order response function Σ_n as the n- order derivative of the local correlation function $\xi(\theta|\kappa_L)$ w.r.t the local convergence κ_L:

$$\Sigma_n(\theta_{12}) = \frac{1}{\xi(\theta_{12})} \frac{d^n\xi(\theta_{12}|\kappa_L)}{d\kappa_L^n} \quad (3.29b)$$

Using Eq.(4.8) in combination with Eq.(3.29a) we can express $\Sigma_n(\theta_{12})$ in terms of $\mathcal{Q}_n(\ell)$ which both carry equivalent information:

$$\Sigma_n(\theta_{12}) = \frac{1}{\xi(\theta_{12})} \frac{1}{4\pi} \sum_{\ell=0}^{\ell_{max}} (2\ell+1)\mathcal{C}_\ell \mathcal{Q}_n(\ell)P_\ell(\cos\theta_{12}).$$

$$\approx \frac{1}{2\pi} \sum_{\ell=0}^{\ell_{max}} \ell J_0(\ell\theta_{12})\mathcal{C}_\ell Q_n(\ell). \quad (3.29c)$$

The second equality is valid in the flat-sky approximation. The lowest-order response function for two-point correlation functions was studied recently in [54, 56–59]. In Figure-4 we show $\Sigma_n(\theta_{12})$ which will be discussed in §6.

4 Response Functions for 3D Weak Lensing

A method to use photometric redshifts to study three-dimensional weak lensing was introduced in [60]. Subsequently, this technique was developed by many authors see, e.g.,[61, 62]. Here we generalise the concept of global 3D shear power spectrum to a local one. The *local shear power spectrum* denoted as $\mathcal{C}_\ell^{\gamma\gamma}(r_1, r_2|\kappa_{L1}, \kappa_{L2})$ is given by:

$$\mathcal{C}_\ell^{\gamma\gamma}(r_1, r_2|\kappa_{L1}, \kappa_{L2}) = \frac{9\Omega_M^2 H_0^4}{16\pi^4 c^2} \frac{(\ell+2)!}{(\ell-2)!} \int \frac{dk}{k^2} V_\ell^\gamma(r_1, k|\delta_L) V_\ell^\gamma(r_2, k|\delta_L); \quad (4.1a)$$

$$\kappa_{Li} = \delta_{Li}|\kappa_{mi}|; \quad \kappa_{mi} = -\int_0^{r_{si}} dr D_+(r) W_i(r). \quad (4.1b)$$

Here, κ_{mi}, i.e. the minimum value of κ_{Li} depends on the radial distance r_i both through the maximum of the integration as well as through the weight W_i. Notice that the global 3D spectrum $\mathcal{C}_\ell^{\gamma\gamma}(r_1, r_2)$ is recovered for $\delta_L = 0$ in which limit $\kappa_{Li} = 0$. The spectroscopic surveys can measure the radial distances with higher accuracy but typically for fewer objects.
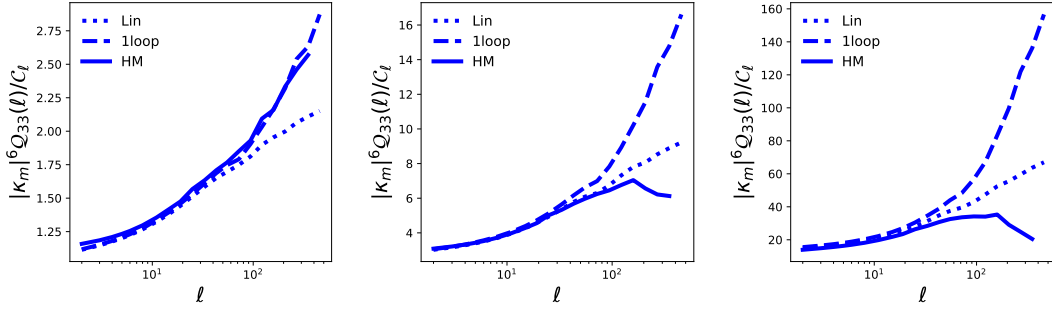
Figure 6: The 3D response functions $|\kappa_m|^{\alpha+\beta}Q_{\alpha\beta}$ defined in Eq.(4.9) are shown for the source redshift $z_s = 1.0$. From left to right panels depict $|\kappa_m|^2 Q_{11}$, $|\kappa_m|^4 Q_{22}$ and $|\kappa_m|^6 Q_{33}$. Various line styles correspond to different analytical models, linear (dashed), one-loop (dotted) and halo model (solid) as indicated.
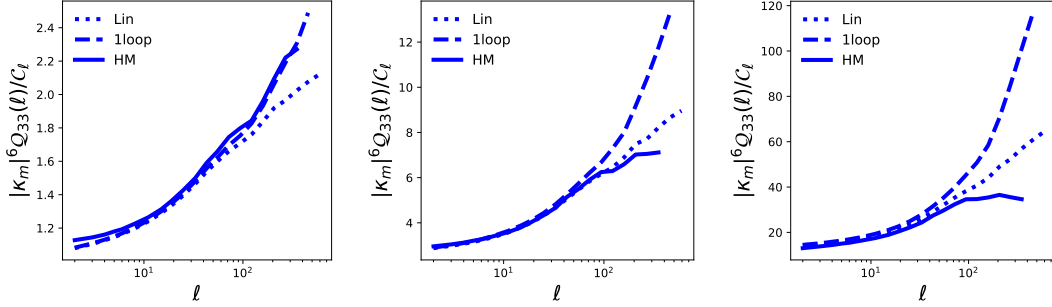

Figure 7: Same as Fig-6 but for $z_s = 2.0$

.

In comparision photometric surveys target a higher number of galaxies, but in general with larger redshift uncertainities. The formalism here is suitable for photometric surveys. The quantities V^γ in Eq.(4.1a) is expressed using a new function U_ℓ

$$V_\ell^\gamma(r_i, k|\delta_L) \equiv \int dz_p\, dz'\, n(z_p)\, p(z'|z_p) W_i U_\ell(r[z_p], k); \tag{4.2a}$$

$$U_\ell(r[z], k|\delta_L) \equiv \int_0^r dr'\, a^{-1}(r') \frac{(r - r')}{rr'} j_\ell(kr') P^{1/2}(k; r'|\delta_L). \tag{4.2b}$$

Here, j_ℓ is the spherical Bessel Function of order ℓ. The cross-power spectrum involving two different redshifts (equivalently, two different radial distances) is often factorized using the corresponding geometric mean, i.e., $P_\delta(k, r_1, r_2) = [P_\delta(k, r_1) P_\delta(k, r_2)]^{1/2}$. This approximation reduces a higher-dimensional integral to a product of lower-dimensional integrals. The accuracy of this ansatz was scrutinized in [63] in the context of weak lensing and was found to be at the level of 10% for scales $k > 5h^{-1}$Mpc. However notice that, using Zeldovich

Approximation ref.[64], it was shown that higher accuracy can be achieved. Indeed, we have a generalised the factorization scheme by adopting it for local power spectrum, i.e., $P_\delta(k, r_1, r_2|\delta_L) = [P_\delta(k, r_1|\delta_L)P_\delta(k, r_2|\delta_L)]^{1/2}$. Next, by Taylor expanding $P_\delta^{1/2}(k, t|\delta_L)$:

$$P^{1/2}(k, t|\delta_L) = P^{1/2}(k, t) \sum_{n=0}^{\infty} \frac{\delta_L^n}{n!} T_n(k, t). \tag{4.3}$$

The coefficients T_n can be expressed in terms R_n using Eq.(4.3).

$$T_1 = \frac{1}{2}R_1; \tag{4.4a}$$

$$T_2 = -\frac{1}{2}R_1^2 + R_2; \tag{4.4b}$$

$$T_3 = \frac{3}{8}R_1^3 - \frac{3}{4}R_1 R_2 + \frac{1}{2}R_3. \tag{4.4c}$$

In Figure-5 we show our results for T_N. The discussions will be presented in §6. It is expected that the radius of convergence for the Taylor expansion of $T^{1/2}$ will be smaller than the original Taylor expansion of T. We will also Taylor expand the functions U_ℓ and V_ℓ:

$$U_\ell(k, t|\delta_L) = \sum_{n=0}^{\infty} \frac{\delta_L^n}{n!} U_\ell^{(n)}(k, t); \quad V_\ell(k, t|\delta_L) = \sum_{n=0}^{\infty} \frac{\delta_L^n}{n!} V_\ell^{(n)}(k, t). \tag{4.5}$$

This will allow use to express the coefficients U_ℓ in terms of the response functions T_α, and subsequently R_α.

$$U_\ell^{(n)}(k, t) = \frac{1}{|\kappa_m|^n} \int_0^r dr' a^{-1}(r') \frac{(r - r')}{rr'} j_\ell(kr') T_n(k, t) P^{1/2}(k; r'). \tag{4.6}$$

Using the Limber approximation (see [65] for a detailed derivation and relation to other such interrelated approximation. e.g.,flat-sky approximation as well as next-to-leading-order corrections to the Limber approximation) $\lim_{\ell \to \infty} j_\ell(x) = \sqrt{\frac{\pi}{2(\ell+1/2)}} \delta_D(\ell + 1/2 - x)$ we can simplify this to the following form [66]:

$$U_\ell^{(n)}(r, k) = \frac{1}{|\kappa_m|^n} \frac{r - \mathcal{L}(k)}{ka(\mathcal{L}(k))r\mathcal{L}(k)} \sqrt{\frac{\pi}{2(\ell + 1/2)}} T^n(k, \mathcal{L}(k)) P^{1/2}(k, \mathcal{L}(k)); \tag{4.7}$$

where we have used the following shorthand notation: $\mathcal{L}(k) = (\ell + 1/2)/k$. A less accurate approximation is also used $\lim_{\ell \to \infty} j_\ell(x) = \sqrt{\frac{\pi}{2\ell}} \delta_D(\ell - x)$, which amounts to using $\mathcal{L}(k) = \ell/k$. Taylor expanding the power spectrum in a bivariate series we define the response functions for the 3D power spectrum:

$$\mathcal{C}_\ell^{\gamma\gamma}(r_1, r_2|\kappa_{L1}, \kappa_{L2}) = \sum_{a,b=0}^{\infty} \frac{1}{a!} \frac{1}{b!} \mathcal{Q}_{ab}(r_1, r_2, \ell) \, \kappa_{L1}^a \kappa_{L2}^b \, \mathcal{C}_\ell^{\gamma\gamma}(r_1, r_2). \tag{4.8}$$

The 3D response functions $\mathcal{Q}_{ab}$ of order ab is a function of two source redshifts r_1 and r_2 and are given by:

$$\mathcal{Q}_{ab}(r_1, r_2, \ell) = \frac{9\Omega_M^2 H_0^4}{16\pi^4 c^2} \frac{(\ell+2)!}{(\ell-2)!} \int \frac{dk}{k^2} V_\ell^a(r_1, k) V_\ell^b(r_2, k). \tag{4.9}$$

For specific forms for the radial distribution of galaxies denoted by $n(z)$ and photometric smoothing $p(z|z_p)$ see [67] which we have ignored. We will also take $r_1 = r_2$. For the results shown for $\mathcal{Q}_{ab}$ in Figure-6 and Figure-7, we assume a single source redshift ($z_s = 1$ or 2) instead of the source distribution. We also neglect the photo-z error and replaced $p(z|z_p)$ it with a delta function.

5 k-cut Response Functions

As is well known, the cosmic shear statistics is very sensitive to small scale power which depends on poorly understood nonlinear physics as well as baryonic feedback. Many techniques have been developed from brute force N-body simulation to model small scale behaviour with subsequent marginalisation over small scale power spectra to develop emulator based approach that can be combined with fast Monte Carlo Markov Chain schemes. However, each of this techniques are either too expensive or lacks sufficient accuracy required for stage-IV experiments.

A solution to this problem was first proposed in [62] (see also [67]) that is geometric in nature and cuts out the weak lensing spectrum's sensitivity to small scale structure in a tunable power. We will refer to the power spectra computed in this manner as k-cut power spectra. This method relies on a nulling scheme that is achieved by applying a similarity transform to the weak lensing spectra following [68]. The key aspect of this transformation is that it organises the lensing information in the lens plane instead of the source plane. Next, taking advantage of the fact that each bin constructed in this manner corresponds to a particular lens redshift range, so taking an angular scale cut thus also removes sensitivity to large-k (small scales) in a uniform manner. In this section we generalise the idea idea of k-cut spectra to k-cut response functions [67, 68].

If we consider a set of discrete source planes at radial distances r_i,

$$\tilde{W}_\alpha(r) = \sum_i p_\alpha^i W_i = \frac{3\Omega_M H_0^2}{2c^2} a^{-1}(r) \sum_{i;\, r_i > r} p_\alpha^i \frac{d_A(r_i - r) d_A(r)}{d_A(r_i)}, \tag{5.1}$$

where $\{p_i\}$ are a set of weights associated with source planes. The key step in implementing the nulling scheme introduced in [68] is to select weights in such a manner that is the weighted convergence $\tilde{\kappa}_\alpha$ is only sensitive to lenses in a specific radial distance.

$$\tilde{\kappa}_\alpha = \sum_i p_\alpha^i \kappa_i. \tag{5.2a}$$

In the harmonic domain:

$$\tilde{\kappa}_{\alpha,\ell m} = \sum_i p_\alpha^i \kappa_{i,\ell m}; \tag{5.2b}$$

We will refer to above transformation as the Bernardeau-Nishimichi-Taruya (BNT) transformation, and $\tilde{\kappa}_a$ as BNT transformed convergence. It can be shown that the BNT weighted power spectra denoted as $\tilde{\mathcal{C}}_\ell^{\alpha\beta} \equiv \langle \kappa_{\ell m}^\alpha \kappa_{\ell m}^{\beta*} \rangle$ is related to the ordinary tomographic spectra $\mathcal{C}_\ell^{ij} \equiv \langle \kappa_{\ell m}^i \kappa_{\ell m}^{*j} \rangle$ through the following similarity (BNT) transformation.

$$\tilde{\mathcal{C}}_\ell^{\alpha\beta} = \sum_{i,j} p_\alpha^i p_\beta^j \mathcal{C}_\ell^{ij}. \tag{5.3}$$

In a more compact matrix notation we can express the similarity transform as:

$$\tilde{\mathbf{C}}_\ell = \mathbf{M} \mathbf{C}_\ell \mathbf{M}^T. \tag{5.4}$$

Construction of the transformation matrix $\mathbf{M}$ from the weights p_α^i, which satisfies various constraints, is detailed in [67, 68].

$$\tilde{\mathcal{C}}_\ell^{\alpha\beta}(\tilde{\kappa}_{LX}) = \sum_{n=0}^{\infty} \frac{1}{n!} \, \tilde{\mathcal{Q}}_n^{\alpha\beta}(\ell) \, \tilde{\kappa}_{LX}^n \tilde{\mathcal{C}}_\ell^{\alpha\beta}. \tag{5.5}$$

This is the BNT equivalent of Eq.(2.3). We can now define the position dependent BNT transformed tomographic spectra $\tilde{\mathcal{C}}_\ell^{\alpha\beta}(\tilde{\kappa}_{LX})$ that depends on $\tilde{\kappa}_{LX} \equiv [\tilde{\kappa}_{L\alpha}\tilde{\kappa}_{L\beta}]^{1/2}$. Going through the algebra we find the equivalent of Eq.(3.11):

$$\tilde{Q}_n^{\alpha\beta}(\ell) = \frac{1}{\mathcal{C}_\ell^{\alpha\beta}} \frac{1}{|\tilde{\kappa}_{LX}|^n} \int_0^{r_s} d\tilde{r} \frac{W^\alpha(r) W^\beta(r)}{d_A^2(r)} R_n \left[\frac{\ell}{d_A(r)}, r \right] [D_+(r)]^n P_\delta \left(\frac{\ell}{d_A(r)}, r \right). \tag{5.6}$$

The corresponding expression for tomographic binning is given in Eq.(3.11). Notice the normalisation of the k-cut response function $\tilde{Q}_\ell^{\alpha\beta}$ is different from that of the ordinary response functions $Q_\ell^{\alpha\beta}$. The following definitions were used to express $\tilde{\kappa}_{LX}$:

$$\tilde{\kappa}_{\alpha L} = \delta_L |\kappa_{\alpha m}|; \qquad \tilde{\kappa}_{\alpha m} = \sum_i p_\alpha^i \kappa_{im}(r) = -\int_0^{r_s} dr \, D_+(r) \sum_i p_i w_i(r). \tag{5.7a}$$

Applying a suitable ℓ cut-off in Eq.(3.11) we can systematically remove the high-k modes. '

6   Results and Discussions

In Figure-1 we show the response functions Q_N defined in Eq.(3.11) are shown. From left-to right panels depict $N = 1, 2$ and $N = 3$. The source redshift is at $z_s = 1$. Various line-styles correspond to different analytical models, linear, one-loop and halo model as indicated. In Figure-2 we present the corresponding results for the source redshift $z_s = 2.0$. The predictions

from one-loop SPT for lower order response functions show relatively better agreement with the HM models

Typically, for the intermediate range of ℓ values most models show an increasing trend. While the halo model predictions show a declining trend at higher-ℓ the predictions based on 1-loop saturates at a rather high value. The predictions based on linear theory are relatively more stable. While each of these predictions need to be checked against simulations for accuracy, it is clear that the response function based approach can probe squeezed bi- or trispectrum and relatively easily to implement compared to the full analysis of higher-order spectra.

The linear and 1-loop corrections are not expected to be valid in the high-ℓ regime as they are unable to probe the nonlinear physics of gravitational clustering. The disagreement is more pronounced at lower redshift as at a lower redshift weak lensing probes higher-level of nonlinearity in the background perturbations. The linear and quasilinear 1-loop power spectra diverge more rapidly. The departure from HM is pronounced even at relatively lower ℓ. The deviations also increase with the order N of the response functions. We have used the linear and 1-loop predictions as a reference. The HM models are expected to be more accurate.

In Figure-3 we show the corresponding response functions for the underlying matter distribution $z = 1$. The response functions R_N defined in Eq.(3.16b)-Eq.(3.16d) are shown. From left to right panels depict $N = 1, 2$ and $N = 3$. For the response function R_1 various models agree with each other for $k < 0.5h\,Mpc^{-1}$. The disagreement among them is more pronounced at lower z and higher N. At low k the two halo term P_{2h} plays a dominant role. The two-halo contributions of HM matches with the linear and quasilinear (1-loop) predictions. However, one-halo term P_{1h} that dominate at smaller scales capture the highly nonlinear physics which is non-perturbative in nature and is not expected to be captured by the quasilinear modelling,

As mentioned before our results correspond to the *tree-level* halo model which is based on the standard tree-level perturbation theory. Recent prescriptions to incorporate EFT based counter-terms in halo model [51] can improve the agreement between the halo model and 1-loop calculations at a relatively high k.

In Figure-4 we show the response functions for the correlation function. The source redshift is fixed at $z_s = 1$. The response functions Σ_N defined in Eq.(3.29c) are shown for the source redshift $z_s = 1.0$. From left to right panels depict $N = 1, 2$ and $N = 3$. Various line styles correspond to different analytical models, linear, one-loop and halo model as indicated. As expected for large separation angle θ all models show similar trends, but they differ in the small separation regime. The results depend on ℓ_{max}. We have used $\ell_{max} = 2000$.

In Figure-5 we have plotted the T_N parameters defined in Eq.(4.4a) - Eq.(4.4c). These coefficients can be obtained by Taylor expanding square roots of the ratio of local and global power spectrum $P^{1/2}(k, r|\delta_L)/P^{1/2}(k, r)$ and are related to the coefficients R_N and are functions of the wave number k. The trends in T_N with z and N is dictated by similar trends in R_N.

The Figure-6 shows 3D response functions for $z_s = 1$ and Figure-7 corresponds to $z_s = 2$. The 3D response function is defined in Eq.(4.8). In 3D the response function depends on two different source redshiftd $z_{s1} = 1$ and $z_{s2} = 2$. From left to right panels depict Q_{11}, Q_{22} and Q_{33}. We show these results for linear theory and 1-loop SPT. In agreement with their projected (2D) counterparts one-loop corrections show departure at increasing lower ℓ. For $z = 1$, halo model show good agreement with 1-loop predictions for $\ell < 300$ Q_{11}. The halo model deviates at an increasing low ℓ with the increase of the order of the response function.

7   Conclusion and Future Prospects

Several authors in recent years have used SU formalism in the context of galaxy clustering studies (e.g. [49, 69, 70]). In this paper we have introduced the response functions approach for analysing the higher-order statistics of weak lensing convergence maps. We have also extended the real space based correlation function results [71] developed for galaxy surveys for the case of weak lensing surveys. The response functions for the correlation functions presented here can be generalised to 3×2 correlation functions typically used to analyse the data from weak lensing surveys. For a different approach to response function see [32].

We have explored the response functions for weak lensing power spectrum. However, the formalism discussed here can be generalised for bispectrum and other higher-order statistics. Separate Universe N-body simulations for dark matter clustering are currently available, but separate universe weak lensing convergence or shear maps from such simulations are currently unavailable. We hope our study will motivate development of such simulations. The validity range of various approximations used in our derivation can then be tested when such simulations become available.

The forward modelling studies based on power spectrum have gained popularity in recent years. These studies can be extended to include the information regarding non-Gaussianity using the response functions introduced here without much additional computational overhead.

To compute the signal-to-noise associated with the response functions we have studied here, the covariance matrices for these statistics is needed, which will be presented in a separate publication.

The preferential alignments of halos due to tidal interactions is responsible for what is also known as intrinsic alignment (IA) and is considered to be a systematics for weak lensing surveys see [72] for KiDS and [73] for DES. It is believed that for analysing the future surveys such as Euclid and LSST it will be vital to understand IA in a lot more detail. Many authors on the other hand have gone a step forward and underlined the usefulness of IA as a cosmological probe. Most statistical modelings of IA is devoted to halo model based approaches. In [53] an effective field theory (EFT) based approach was developed for modelling of power spectrum and in [74] the authors have focused on bispectrum induced by IA. A response function based approach that only relies on modelling of power spectrum [75] and its derivatives will be presented elsewhere.

The theoretical framework developed here will also be useful beyond weak lensing studies in other areas of cosmology, e.g., in the context of Lyman-α [76] absorption studies, 21cm studies [77] and studies of CMB secondaries[78].

Acknowledgment

References

[1] Weak Gravitational Lensing, M. Bartelmann, P. Schneider, 2001, Phys. Rep., 340, 291, [arxiv/9912508]

[2] Cosmology with Weak Lensing Surveys, D. Munshi, P. Valageas, L. Van Waerbeke, A. Heavens, 2008, Phys.Rept., 462, 67, [arxiv/0612667]

[3] *The Hyper Suprime-Cam SSP Survey: Overview and Survey Design,* Aihara H. et al., 2018, Publications of the Astronomical Society of Japan, Volume 70, Issue SP1, S4, [arXiv/1704.05858]

[4] *Cosmology from Cosmic Shear with DES Science Verification Data,* The Dark Energy Survey Collaboration, T Abbott, F. B. Abdalla, S. Allam, et al., 2016, PRD, 94, 022001, [arxiv/1507.0552]

[5] *Gravitational Lensing Analysis of the Kilo Degree Survey,* K. Kuijken, C. Heymans, H. Hildebrandt, et al., 2015, MNRAS, 454, 3500, [astro-ph/1507.00738]

[6] *Euclid Definition Study Report,* R. Laureijs, J. Amiaux, S. Arduini, et al. 2011, ESA/SRE(2011)12.

[7] *LSST: a complementary probe of dark energy,* J. A. Tyson, D. M. Wittman, J. F. Hennawi, D. N Spergel, 2003, Nuclear Physics B Proceedings Supplements, 124, 21, [astro-ph/0209632]

[8] *National Research Council. 2010. New Worlds, New Horizons in A&A. The National Academies Press.*

[9] *Beyond the Cosmological Standard Model,,* A. Joyce, B. Jain, J. Khoury, M. Trodden, 2015, Phys. Rep., 568, 1, [astro-ph/1407.0059]

[10] *Modified Gravity and Cosmology,* T. Clifton, P. G. Ferreira, A. Padilla, S. Skordis, 2012, Phys. Rep., 513, 1, 1, [astro-ph/1106.2476]

[11] *Massive neutrinos and cosmology,* J. Lesgourgues, S. Pastor, 2006, Phys. Rep., 429, 307, [astro-ph/1610.02956]

[12] *Large scale structure of the universe and cosmological perturbation theory,* F. Bernardeau, S. Colombi, E. Gaztanaga, R. Scoccimarro, 2002, Phys.Rep. 367, 1, [astro-ph/0112551]

[13] *The three-point correlation function of cosmic shear: I. The natural components* P. Schneider, M. Lombardi, 2003, A&A, 397, 809 [`arXiv/0207454`]

[14] *The three-point correlation function of cosmic shear. II: Relation to the bispectrum of the projected mass density and generalized third-order aperture measures* P. Schneider, M. Kilbinger, M. Lombardi, 2005, A&A, 431, 9, [`astro-ph/0308328`]

[15] *The Three-Point Correlation Function for Spin-2 Fields* M. Takada, B. Jain, 2003, ApJ, 583, L49 [`arXiv/0210261`]

[16] *Cosmological parameters from weak lensing power spectrum and bispectrum tomography: including the non-Gaussian errors* I. Kayo, M. Takada [`arXiv/1306.4684`]

[17] *Weak lensing from space: first cosmological constraints from three-point shear statistics* E. Semboloni, T. Schrabback, L. van Waerbeke, S. Vafaei, J. Hartlap, S. Hilbert, 2010, MNRAS, 410, 143 [`arXiv/1005.4941`]

[18] *Non-Gaussianity from Inflation: Theory and Observations* N. Bartolo, E. Komatsu, S. Matarrese, A. Riotto 2004, Phys.Rept. 402, 103 [`astro-ph/0406398`]

[19] *Higher order statistics of shear field: a machine learning approach,* C. Parroni, E. Tollet, V. F. Cardone, R. Maoli, R. Scaramella, [`astro-ph/1612.02264`]

[20] *Weak lensing shear and aperture-mass from linear to non-linear scales* D. Munshi, P. Valageas, A. J. Barber MNRAS, 2004, 350, 77 [`astro-ph/1612.02264`]

[21] *Cylinders out of a top hat: counts-in-cells for projected densities* C. Uhlemann, 2018, MNRAS, 477, 2772U, [`arXiv/1711.04767`]

[22] *Cosmological constraints with weak lensing peak counts and second-order statistics in a large-field survey,* A. Peel, C.-A. Lin, F. Lanusse, A. Leonard, J.-L. Starck, M. Kilbinger, 2017, A&A 599, A79, [`arXiv/1612.02264`]

[23] *Weak Lensing Skew-Spectrum,* D. Munshi, T. Namikawa, T. D. Kitching, J. D. McEwen, F. R. Bouchet, 2020, MNRAS, 498, 6057, [`arXiv/2006.12832`]

[24] *Estimating the Integrated Bispectrum from Weak Lensing Maps,* D. Munshi, J. D. McEwen, T. Kitching, P. Fosalba, R. Teyssier, J. Stade,l 2020, MNRAS, 493, 3985, [`arXiv/1902.04877`]

[25] *New Optimised Estimators for the Primordial Trispectrum,* D. Munshi, A. Heavens, A. Cooray, J. Smidt, P. Coles, P. Serra, 2011, MNRAS, 412, 1993, `arXiv/0910.3693`

[26] *Morphology of Weak Lensing Convergence Maps* D. Munshi, T. Namikawa, J. D. McEwen, T. D. Kitching, F. R. Bouchet, [`arXiv/2010.05669`]

[27] *Matter trispectrum: theoretical modelling and comparison to N-body simulations* D. Gualdi, S. Novell, H. Gil-Marín, L. Verde 2021, JCAP, 01, 015 `arXiv/2009.02290,`

[28] *Persistent homology in cosmic shear: constraining parameters* with topological data analysis S. Heydenreich, B. Brück, J. Harnois-Déraps 2021, A&A, 648, 74 `arxiv/2007.13724,`

[29] *Exact Extreme Value Statistics and the Halo Mass Function* I. Harrison, P. Coles MNRAS 418, L20-L24 (2011) `arXiv/1108.1358,`

[30] *The position-dependent matter density probability distribution function* D. Jamieson, M. Loverde 2020, PRD 102, 123546 `arxiv/2010.07235,`

[31] *An adapted filter function for density split statistics in weak lensing* P. Burger, P. Schneider, V. Demchenko, J. Harnois-Deraps, C. Heymans, H. Hildebrandt, S. Unruh 2020, A&A 642, A161 (see also `arXiv/2006.10778`).

[32] *Response function of the large-scale structure of the universe,* to the small scale inhomogeneities, T. Nishimichi, F. Bernardeau, A. Taruya, Physics Letters B, 762, 247, `arXiv/1411.2970`

[33] *The Weak Lensing Bispectrum Induced By Gravity,* D. Munshi, T. Namikawa, T. D. Kitching, J. D. McEwen, R. Takahashi, F. R. Bouchet, A. Taruya, B. Bose, 2020, MNRAS, 493, 3985 `arXiv/1910.04627`

[34] *Phase Correlations in Non-Gaussian Fields* T. Matsubara, 2003, ApJ., 591, L79 [`astro-ph/0303278`]

[35] *Statistics of Fourier Modes in Non-Gaussian Fields* T. Matsubara, 2007, ApJS, 170, 1, [`astro-ph/0610536`]

[36] *A New Estimator for Phase Statistics* D. Munshi, R. Takahashi, J. D. McEwen, T. D. Kitching, F. R. Bouchet, 2022, JCAP, 05, 006, [`arXiv/2109.08047`]

[37] *Higher-order statistics of shear field: a machine learning approach,* C. Parroni, E. Tollet, V. F. Cardone, R. Maoli, R. Scaramella 2021, A&A 645, 123 [`arXiv/2011.10438xs`]

[38] Position-dependent power spectrum: a new observable in the large-scale structure C.-T. Chiang [`arXiv/1508.03257`]

[39] *Planck 2015 results. XIII. Cosmological parameters* Planck Collaboration, 2016, A&A, 594, A13

[40] *Galaxy bias and non-linear structure formation in general relativity* T. Baldauf, U. Seljak, L. Senatore, M. Zaldarriaga, 2011, JCAP, 10, 031

[41] *Power spectrum super-sample covariance* M. Takada, W. Hu, 2013, PRD, 87, 123504

[42] *Responses of Halo Occupation Distributions: a new ingredient in the halo model & the impact on galaxy bias* R. Voivodic, A. Barreirab 2021, JCAP, 05, 069 [`arXiv/0809.5112`]

[43] Efficient Evaluation of Cosmological Angular Statistics V. Assassi, M. Simonović, M. Zaldarriaga, 2017, JCAP, 11, 054, [`arXiv/1705.05022`]

[44] *A Universal Density Profile from Hierarchical Clustering* J. F. Navarro, C. S. Frenk, S. D. M. White, 1997, ApJ, 490, 493 [`arXiv/9611107`]

[45] *Toward a halo mass function for precision cosmology: the limits of universality* J. L Tinker, A. V Kravtsov, A. Klypin, K. Abazajian, M. S Warren, G. Yepes, S. Gottlober, D. E Holz 2008, ApJ, 688, 709 [`arXiv/0803.2706`]

[46] *The Large-scale Bias of Dark Matter Halos: Numerical Calibration and Model Tests* J. L. Tinker, B. E. Robertson, A. V. Kravtsov, A. Klypin, M. S. Warren, G. Yepes, S. Gottlöber, 2010, ApJ, 724, 878 [`arXiv/1001.3162`]

[47] *Precision measurement of the local bias of dark matter halos* T. Lazeyras, C. Wagner, T, Baldauf, F. Schmidt 2016, JCAP, 02, 018 [`arXiv/1511.01096`]

[48] *Dark matter halo concentrations in the Wilkinson Microwave Anisotropy Probe year 5 cosmology* A. R. Duffy, J. Schaye, S. T. Kay, C. Dalla Vecchia, MNRAS, 390L, 64 [`arXiv/0804.2486`]

[49] *The angle-averaged squeezed limit of nonlinear matter N-point functions,* C. Wagner, F. Schmidt, C.-T. Chiang, E. Komatsu, 2015, JCAP, 08, 042 [`arxiv/1503.03487`]

[50] *Halo Models of Large Scale Structure* A. Cooray, R. Sheth 2002, Phys.Rept., 372, 1 [`astro-ph/0206508`]

[51] *The Effective Halo Model: Creating a Physical and Accurate Model of the Matter Power Spectrum and Cluster Counts* O. H. E. Philcox, D. N. Spergel, F. Villaescusa-Navarro 2020, PRD, 101, 123520 [`arXiv/2004.09515`]

[52] Towards a self-consistent halo model for the nonlinear large-scale structure F. Schmidt 2016, PRD, 93, 063512 [`arXiv/1511.02231`]

[53] *Precision Comparison of the Power Spectrum in the EFTofLSS with Simulations* S. Foreman, H. Perrier, L. Senatore 2016, JCAP, 05, 027 [`arXiv/1507.05326`]

[54] *Position-Dependent Correlation Function of Weak Lensing Convergence* D. Munshi, G. Jung, T. D. Kitching, J. McEwen, M. Liguori, T. Namikawa, A. Heavens [`arXiv/2104.01185`]

[55] *Position-dependent correlation function from the SDSS-III Baryon Oscillation Spectroscopic Survey Data Release 10 CMASS Sample* C.-T. Chiang, C. Wagner, A. G. Sánchez, F. Schmidt, E. Komatsu 2015, JCAP, 09, 028 [`arXiv/1504.03322`]

[56] *Response approach to the integrated shear 3-point correlation function: the impact of baryonic effects on small scales* A. Halder, A. Barreira [`arXiv/2201.05607`]

[57] *Accurate cosmic shear errors: do we need ensembles of simulations?* A. Barreira, E. Krause, F. Schmidt 2018, JCAP, 10, 053 [`arXiv/1807.04266`]

[58] *Covariances for cosmic shear and galaxy-galaxy lensing in the response approach* R. Takahashi, T. Nishimichi, M. Takada, M. Shirasaki, K. Shiroyama 2019, MNRAS, 482, 4253 [`arXiv/1805.11629`]

[59] *The integrated 3-point correlation function of cosmic shear* A. Halder, O. Friedrich, S. Seitz, T. N. Varga 2021, MNRAS, 506, 2780 [`arXiv/2201.05607`]

[60] *3D weak lensing* A. F. Heavens, 2003, MNRAS, 343, 1327 [`arXiv/0304151`]

[61] *Weak lensing analysis in three dimensions* P. G. Castro, A. F. Heavens, T. D. Kitching 2005, PRD, 72, 023516 [`astro-ph/0503479`]

[62] *3D Photometric Cosmic Shear* T. D. Kitching, A. F. Heavens, L. Miller 2011, MNRAS, 413, 2923 [`arXiv/1007.2953`]

[63] *Unequal-Time Correlators for Cosmology* T. D. Kitching, A. F. Heavens 2017, PRD, 95, 063522 [`arXiv/1612.00770`]

[64] *Unequal time correlators and the Zeldovich approximation* N. E. Chisari, A. Pontzen 2019, PRD 100, 023543 [`arXiv/1905.02078`]

[65] *Extended Limber Approximation* M. LoVerde, N. Afshordi 2008, PRD, 78, 123506 [`arXiv/0809.5112`]

[66] *Accurate photometric redshifts for the CFHT Legacy Survey calibrated using the VIMOS VLT Deep Survey* O. Ilbert, A&A 2006, 457, 841 [`astro-ph/0603217`]

[67] *k-cut Cosmic Shear: Tunable Power Spectrum Sensitivity to Test Gravity* P. L. Taylor, F. Bernardeau, T. D. Kitching 2018, PRD, 98, 083514 [`arxiv/1809.03515`]

[68] *Cosmic shear full nulling: sorting out dynamics, geometry and systematics,* F. Bernardeau, T. Nishimichi, A. Taruya, 2014, MNRAS, 445, 1526, [`arXiv/1312.0430`]

[69] *Position-dependent power spectrum of the large-scale structure:* a novel method to measure the squeezed-limit bispectrum, C.-T. Chiang, C. Wagner, F. Schmidt, E. Komatsu, 2014, JCAP, 05, 048 [`arxiv/1106.5507`]

[70] *Separate universe approach to evaluate nonlinear matter power spectrum for non-flat ΛCDM model* R. Terasawa, R. Takahashi, T. Nishimichi, M. Takada, 2022, submitted to PRD, [`arxiv/2205.10339`]

[71] *Position-dependent correlation function from the SDSS-III Baryon Oscillation Spectroscopic Survey Data Release 10 CMASS Sample,* C.-T. Chiang, C. Wagner, A. G. Sánchez, F. Schmidt, E. Komatsu, 2015. JCAP, 09, 028, [`arXiv/1504.03322`]

[72] *KiDS-1000 Methodology: Modelling and inference for joint weak gravitational lensing and spectroscopic galaxy clustering analysis,* B. Joachimi, et al., 2021, A&A, 646, A129 [`arXiv/1701.03375`]

[73] *Dark Energy Survey Year 3 Results: Three-Point Shear Correlations and Mass Aperture Moments,* L. F. Secco, et al., 2022, PRD, 105, 023515, [`arXiv/2201.05227`]

[74] *Three-point intrinsic alignments of dark matter halos in the IllustrisTNG simulation,* S. Pyne, A. Tenneti, B. Joachimi, [`arXiv/2204.10342`]

[75] *An EFT description of galaxy intrinsic alignments,* Z. Vlah, C. N. Elisia, F. Schmidt, 2020, JCAP, 01, 025,

[76] *Response approach to the squeezed-limit bispectrum: application to the correlation of quasar and Lyman-α forest power spectrum,* C-T Chiang, A. M. Cieplak, F. Schmidt, A. Slosar, 2017, JCAP 06, 0220, [`arXiv/1701.03375`]

[77] *The large-scale 21-cm power spectrum from reionization,* I. Georgiev, G. Mellema, S. K. Giri, R. Mondal, [`arXiv/2110.13190`]

[78] *Extracting the late-time kinetic Sunyaev-Zel'dovich effect,* D. Munshi, I. T. Iliev, K. L. Dixon, P. Coles, 2016, MNRAS, 463, 2425, [`arXiv/1511.03449`]

[79] *The Integrated Bispectrum and Beyond* D. Munshi, P. Coles 2017, JCAP, 02, 010 [`arXiv/1608.04345`]

A   Perturbative Results

Following [79], the expression for the exact 2D expression is given by:

$$S_3(\ell) = N_2 \left[\frac{24}{7} - \frac{1}{2}(n+1) \right] \tag{A.1a}$$

$$N_2 = \int_0^{r_s} dr \, \frac{W^3(r)}{d_A^{4+2n}(r)} \Big/ \left(\int_0^{r_s} dr \, \frac{W(r)}{d_A^{4+2n}(r)} \right)^2 \tag{A.1b}$$

and also the doubly squeezed trispectrum is given by:

$$S_3(\ell) = N_3 \left[\frac{1473}{79} - \frac{195}{14}(n+2) + \frac{3}{4}(n+2)^2 \right] \tag{A.2a}$$

$$N_3 = \int_0^{r_s} dr \frac{W^4(r)}{d_A^{6+3n}(r)} \bigg/ \left(\int_0^{r_s} dr \frac{W^2(r)}{d_A^{6+3n}(r)} \right)^2 \tag{A.2b}$$